Phys. Med. Biol. **42** (1997) 2015–2025. Printed in the UK PII: S0031-9155(97)83071-0

Diffraction enhanced x-ray imaging

D Chapman†‡, W Thomlinson§, R E Johnston‖, D Washburn‖, E Pisano‖, N Gmür§, Z Zhong§, R Menk¶, F Arfelli+ and D Sayers*

† CSRRI, Illinois Institute of Technology, 3101 South Dearborn, Chicago, IL 60616, USA
§ National Synchrotron Light Source, Brookhaven National Laboratory, Upton, NY 11973, USA
‖ University of North Carolina, Chapel Hill, NC 27599, USA
¶ Universität GHS Siegen, 57068 Siegen, Germany
+ Società Sincrotrone Trieste e Sezione dell' INFN -Trieste, Italy
* Physics Department, North Carolina State University, Raleigh, NC 27695, USA

Received 1 April 1997, in final form 4 August 1997

Abstract. Diffraction enhanced imaging is a new x-ray radiographic imaging modality using monochromatic x-rays from a synchrotron which produces images of thick absorbing objects that are almost completely free of scatter. They show dramatically improved contrast over standard imaging applied to the same phantom. The contrast is based not only on attenuation but also the refraction and diffraction properties of the sample. This imaging method may improve image quality for medical applications, industrial radiography for non-destructive testing and x-ray computed tomography.

1. Introduction

Diffraction enhanced imaging (DEI), is a new x-ray radiographic imaging modality which is a product of a research programme designed to explore a monoenergetic line scan system for radiography of thick absorbing objects (Johnston *et al* 1996). The x-ray source is from the X27C beamline at the National Synchrotron Light Source. Synchrotron radiation provides x-rays which are intense, vertically collimated, polarized and continuous over a wide energy range (Margaritondo 1988). These highly desirable qualities allow a wide variety of imaging research to be performed at a synchrotron (Thomlinson 1992, 1994).

For this study a crystal monochromator is used to select a small energy band from the incident synchrotron radiation which forms the imaging beam which strikes the object. One aspect of this programme has been the use of an additional crystal similar to the type used in the monochromator as a scatter rejection optic that diffracts the beam which is transmitted through the object being imaged. This additional crystal is called an analyser crystal or just analyser. Experiments performed with the analyser revealed that this system was sensitive to refractive index effects within the object in addition to the x-ray absorption and scattering by the object. The early experiments indicated that from two images acquired using an analyser crystal a simple algorithm could be used to separate refractive index effects from the absorption effects (Chapman *et al* 1996). These pilot experiments were performed using a transmission case (Laue geometry) analyser to simultaneously obtain a transmission image and a diffracted image.

‡ E-mail address: chapman@sparky.csrri.iit.edu

0031-9155/97/112015+11$19.50

Definitive experiments and analysis have now been performed to explore the use of a reflection case (Bragg geometry) analyser crystal arrangement to decompose two diffracted images into an independent refraction image and an apparent absorption image. Apparent absorption means the combined absorption and extinction processes. Extinction is the loss of intensity due to diffraction occurring as the beam traverses the object. The type of extinction referred to is commonly called secondary extinction (Zachariasen 1963). Images taken with the new system are presented which show contrast at least an order of magnitude greater than the measured values for synchrotron x-ray images of the same object acquired using the conventional transmission imaging modality. These images are of thick objects containing at least a 36 mm acrylic plastic thickness. In fact, images from this new modality show additional information that is not available with standard radiography.

An algorithm is presented here for the case of a Bragg analyser which can be used to decompose the images into separate refraction and apparent absorption components. The same algorithm can be applied to the diffracted images in the Laue case. The diffracted images are essentially scatter free, since the crystal prevents much of the scatter from reaching the detector. The refraction image is shown to have high sensitivity for delineating the boundaries of those regions in the object which have different refractive indices. An explanation of the sources of the enhanced image contrast is also given which shows that the increased contrast is a result of extinction effects. This opens new opportunities for imaging based on these properties. Since the contrast of an image based on extinction can be much higher than contrast based on x-ray attenuation, detection of smaller inhomogeneities like tumours in medical images or microfractures in industrial parts should be feasible.

The ability of the monochromator and analyser system to resolve refraction effects does not depend on the imaging energy. However, the scattering properties of various elements are energy dependent, which may allow optimization of the imaging system energy to maximize contrast due to extinction while maintaining refraction contrast. Thus, the new modality may be optimally applied at higher x-ray energies, which would allow for better penetration in non-destructive testing or lower doses in medical imaging.

Other researchers have applied diffractive optics to imaging problems (Beliaevsky *et al* 1991, Somenkov *et al* 1996, Podurets *et al* 1989) and have observed refraction effects. However, the method described here quantifies and produces images of the refraction and absorption independently for the first time. Recently, there has been interest in phase contrast imaging which makes use of the high transverse coherence of third-generation synchrotron sources. Phase contrast images are limited to either thin objects or high x-ray imaging energies (Davis *et al* 1995, Nugent *et al* 1996, Wilkins *et al* 1996). The DEI technique in the present work does not depend on phase contrast and works with thick samples.

2. Physical principles of DEI

A radiograph using monoenergetic x-rays contains several components: a coherently scattered component, an incoherently scattered component, and the transmitted beam. Part of the transmitted beam may be refracted in the sample through a very small angle (microradians) due to refractive index gradients in the object. In the x-ray range refractive index gradients arise from variations in ρt along the beam path, where ρ is the density and t is the thickness. A fraction of the transmitted beam may also be diffracted by organized structures within the sample through angles of the order of milliradians (small-angle scattering). I_C, I_I, and I_D are the portions of the coherent scattering, incoherent scattering and diffraction intensity which arrive on the detector along with I_R. I_R is the portion of the incident beam which has only been affected by refraction and attenuated by

absorption and extinction. The recorded intensity, I_N, in a radiograph can be expressed as

$$I_N = I_R + I_D + I_C + I_I. \tag{1}$$

Variations in I_N across the field of view of the detector are the sources of contrast in normal radiography (formally $\Delta I_N/I_N$). The DEI modality will separate I_R from the other components and will show contrast based on refraction, absorption and extinction.

The scattering components, I_C and I_I, contribute to loss of contrast and spatial resolution. Some improvement can be obtained by using synchrotron radiation and a monochromator to select the energy (Johnston *et al* 1996, Burattini *et al* 1994). However, it has been shown that considerable additional gain in contrast can be realized by adding crystal diffraction optics between the object and the imaging system. This refinement almost completely removes the scatter contribution to the image since only x-rays aligned within the angular acceptance of a crystal analyser will be diffracted onto the detector. I_C and I_I are eliminated as contributions to the image. The angular acceptance is called the rocking curve of the crystal (Zachariasen 1945). For the x-ray energies and crystal reflections used here, the width of this curve is a few microradians.

Since the diffraction angles in the sample being imaged are typically a few milliradians (small-angle scattering), most of I_D is rejected by the crystal. It is this rejection of small-angle scattering in particular which gives rise to the sensitivity to the loss of direct beam intensity which has been 'small-angle scattered'. In diffraction research, the term used for the loss of direct beam intensity due to scattering is secondary extinction (Zachariasen 1945, 1963). Normally, the small-angle scattered x-rays will not be distinguished from the direct beam and will appear in a radiograph of the object. Thus in normal radiography there will be no extinction contrast.

The rejection of the scattered x-rays leaves only I_R, the intensity of x-rays transmitted through the sample with a direction very close to the initial direction of the beam. This beam may have been refracted slightly as it passes through the sample (of the order of microradians).

In DEI two images are acquired, one on each side of the rocking curve of the Bragg analyser. Each image contains information about the object's apparent absorption and refraction. Since the analyser crystal orientation is chosen to diffract the beam in the vertical plane, it is sensitive only to the vertical component, $\Delta\theta_Z$, of the refracted x-rays.

The intensity diffracted by the analyser set at a relative angle θ from the Bragg angle θ_B where $\theta_B + \theta$ is the angle between the incident beam and diffraction planes and is given by

$$I_B = I_R R(\theta_B + \theta) \tag{2}$$

where $R(\theta)$ is the analyser reflectivity.

For DEI the analyser is set to $\theta = \pm\Delta\theta_D/2$ where $\Delta\theta_D$is the full width at half maximum of the rocking curve (Darwin width). This is the point of steepest slope of the rocking curve. For an incident x-ray which is not deviated in passing through the sample and incident upon the analyser at this angle the reflectivity will be 0.5. If the x-ray emerging from the object is refracted by $\Delta\theta_Z$ then the diffracted intensity will be

$$I_B = I_R R\left(\theta_B \pm \frac{\Delta\theta_D}{2} + \Delta\theta_Z\right). \tag{3}$$

For refracted x-rays there will be a variation in intensity due to the slope of the rocking curve. For example, with $\Delta\theta_D/2$ positive (high-angle side) a beam refracted with $\Delta\theta_Z > 0$ is diffracted by the analyser with reflectivity less than 0.5. A beam refracted with $\Delta\theta_Z < 0$ is diffracted by the analyser with reflectivity greater than 0.5. If the alignment of the

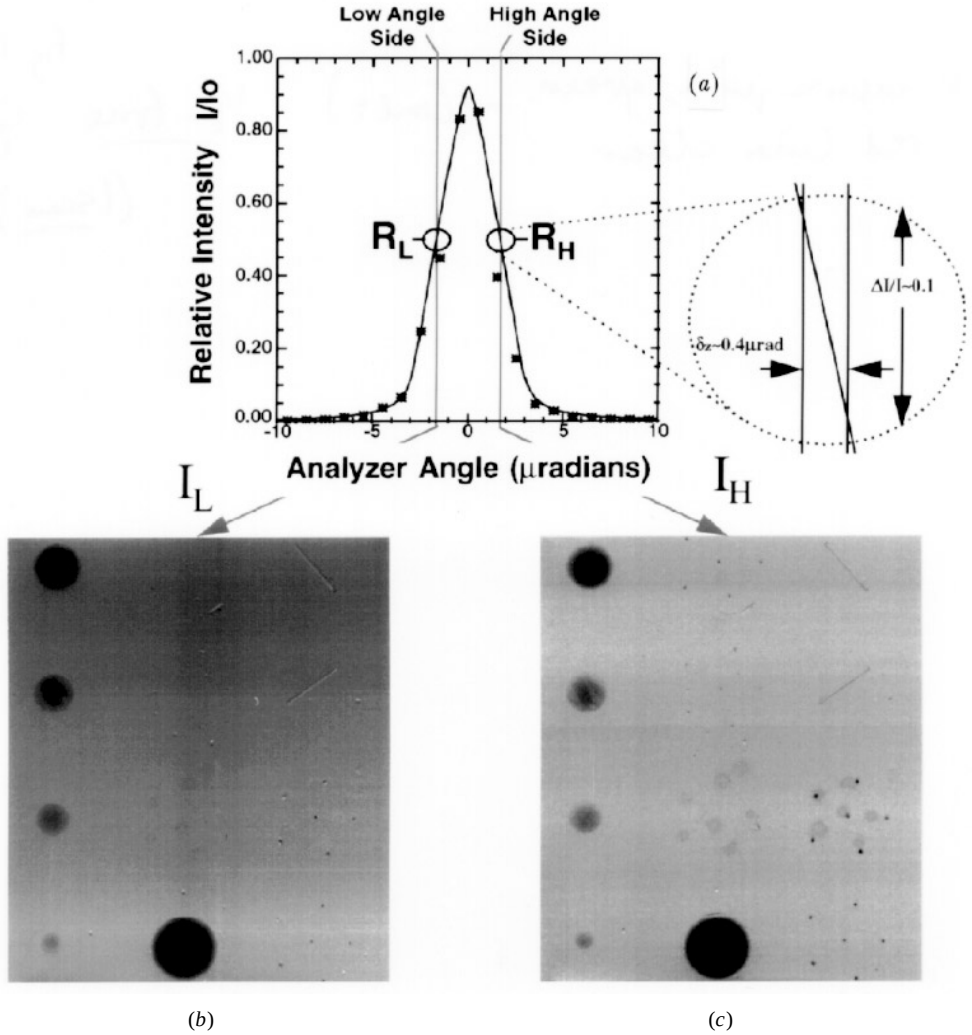

Figure 1. (*a*) The Si (3, 3, 3) analyser rocking curve at 18 keV (full curve, calculated; stars, measured points). The calculation includes the effects of the beam diffracted by the double-crystal monochromator. An image is taken on each side of the peak, shown by the vertical lines. Any refraction near these vertical lines is varied in intensity due to the slope of the rocking curve, as shown in the inset. The range of refraction angles occurring in the ACR phantom is ± 0.2 μrad, creating intensity variations of $\pm 5\%$. (*b*) The intensity recorded on the image plate using the low-angle side of the rocking curve. (*c*) The high-angle side image. Notice that the contrast of the fibrils has switched between the two images.

analyser crystal was such that $\Delta\theta_D/2$ was negative (low-angle side) this effect would be reversed since the derivative of the rocking curve, $\mathrm{d}R/\mathrm{d}\theta$, is of opposite sign. The steeper the slope, the greater the intensity variation due to refraction effects in the two images. For a deviation of more than $\Delta\theta_D/2$ the reflectivity will not be unique and refraction effects cannot be resolved. This is shown in figure 1(a) which shows the locations on the rocking curve where the images are taken. Also shown in figure 1 are images taken on the high- and low-angle sides of the rocking curve which will be discussed

later. In the regions of the phantom which were imaged, the refraction angles were within ± 0.2 μrad, placing all possible angles within a limited region of the rocking curve (about 5 μrad).

At $\pm\Delta\theta_D/2$ where the slope of the rocking curve is fairly constant and for small values of $\Delta\theta_Z$, $R(\theta_0 + \Delta\theta_Z)$ can be expressed as a two-term Taylor series approximation

$$R(\theta_0 + \Delta\theta_Z) = R(\theta_0) + \frac{\mathrm{d}R}{\mathrm{d}\theta}(\theta_0)\Delta\theta_Z. \tag{4}$$

The intensity of the images taken on the low-angle side (θ_L) and the high-angle side (θ_H) of the rocking curve are

$$I_L = I_R\left(R(\theta_L) + \frac{\mathrm{d}R}{\mathrm{d}\theta}(\theta_L)\Delta\theta_Z\right) \tag{5a}$$

$$I_H = I_R\left(R(\theta_H) + \frac{\mathrm{d}R}{\mathrm{d}\theta}(\theta_H)\Delta\theta_Z\right). \tag{5b}$$

These two equations can be solved for the intensity affected by apparent absorption, I_R, and for the refraction angle image, $\Delta\theta_Z$, the angle through which I_R is refracted in the z direction in traversing the object. The solutions are

$$I_R = \frac{I_L\left(\frac{\mathrm{d}R}{\mathrm{d}\theta}\right)(\theta_H) - I_H\left(\frac{\mathrm{d}R}{\mathrm{d}\theta}\right)(\theta_L)}{R(\theta_L)\left(\frac{\mathrm{d}R}{\mathrm{d}\theta}\right)(\theta_H) - R(\theta_H)\left(\frac{\mathrm{d}R}{\mathrm{d}\theta}\right)(\theta_L)} \tag{6a}$$

$$\Delta\theta_Z = \frac{I_H R(\theta_L) - I_L R(\theta_H)}{I_L\left(\frac{\mathrm{d}R}{\mathrm{d}\theta}\right)(\theta_H) - I_H\left(\frac{\mathrm{d}R}{\mathrm{d}\theta}\right)(\theta_L)}. \tag{6b}$$

This algorithm is applied on a pixel-by-pixel basis to the diffracted images from the high- and low-angle side of the rocking curve.

3. Methods

The experiments were performed at the X27C beamline at the National Synchrotron Light Source (NSLS) at Brookhaven National Laboratory. The experimental set-up is shown in figure 2. The white synchrotron beam was made nearly monochromatic by a silicon double-crystal monochromator which is located approximately 22 m from the source of

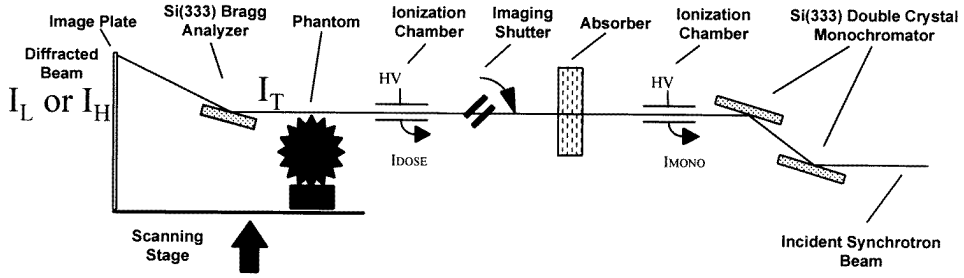

Figure 2. A schematic diagram of the Bragg geometry set-up in the X27C experimental hutch at the NSLS. The image in figure 1(*b*) was made using a similar set-up, only without the Bragg crystal analyser in place. Not shown in the diagram are the sets of collimators just before the sample and just before the image plate, which help to reduce air scatter and scatter from the sample reaching the detector.

radiation. The tunable energy range of this system was 16–25 keV. For the measurements described here the beam energy was 18 keV with an energy width of about 1.5 eV. The monochromator crystals used the silicon $(3, 3, 3)$ lattice planes. This choice of lattice planes increased the sensitivity to refraction effects by a factor of five from the previous experiments that used the $(1, 1, 1)$ lattice planes because of the narrower rocking curve of the $(3, 3, 3)$ reflection (Chapman *et al* 1996). The imaging beam was approximately 80 mm wide and 0.1 mm high at the location of the object. The beam passed through a gas ionization chamber, used for monitoring the intensity of the direct beam, and a set of Lucite absorbers that reduced the beam intensity. A rotary shutter was used to control the exposure and limit unnecessary scatter at the detector position. A second ion chamber was used to measure the radiation exposure at the surface of the object. Images taken with and without the analyser were at exposure levels comparable to conventional mammography x-ray systems. The object to be imaged was mounted on a scanning stage that was driven by a stepping motor. The x-ray beam transmitted through the object could be either imaged directly as in normal radiography or following diffraction in the vertical plane by the silicon Bragg analyser. Radiation exposure to the image plate was controlled by adjusting the scan speed to maintain an exposure of about 1.3 μC kg^{-1} (5 mR) to the plate. Typical scanning times for these experiments were on the order of 4 to 200 s. These limits were dictated by our scanning motors and mechanical system.

The synchrotron images were obtained by maintaining a nearly constant exposure ($\sim$1.3 μC kg^{-1}) to the image plate. In acquiring the DEI images the phantom was exposed to four times the exposure of the non-analyser synchrotron radiographs. A factor of two in increased exposure compensates for the 0.5 reflectivity of the Bragg analyser crystal and another factor of two increased exposure compensates for the two images on each side of the rocking curve.

The detector was a photo stimulative phosphor image plate, typically used for radiology (Fuji Medical Systems high-resolution HR5 and standard resolution ST5 image plates). The image recorded on the plate was digitized, stored and displayed by a Fuji Medical Systems AC3 reader and workstation. The image plates were read out at 2560×2048 matrix size which results in an image of 100 μm per pixel (0.1×0.1 mm^2).

The diffraction angle of the analyser crystal could be finely tuned using a stepper-motor driven translation stage pushing on a long bar attached to an axle to which the crystal was attached (tangent arm). The resolution limit of the tangent arm was 1 μrad which was sufficient for placing the Bragg analyser crystal at a selected position on its rocking curve.

Because the initial interest was in studying the use of synchrotron imaging for early detection of breast cancers, a mammography phantom was used as the test object to be radiographed. The standard phantom used for quality control in mammography is the American College of Radiology (ACR) phantom manufactured by Gammex RMI: Model 156. It contains features which simulate lesions commonly found in breast tissue, namely tumour-like masses (lens-shaped objects of different thicknesses and diameters), simulated microcalcifications arranged as vertices of five-point stars and cylindrical nylon fibrils (Johnston *et al* 1996, Arfelli *et al* 1995). The features are fixed in a wax block contained in a thick acrylic base. This phantom approximates a 40 to 45 mm thick compressed breast. Since the x-ray beam is a fan in the horizontal plane (x–y plane), the object and the image plate were simultaneously translated in the vertical direction (z-direction). This scanning was accomplished by a computer-controlled stepper-motor translation stage which held both the phantom support and a mount for the image plate cassette.

4. Results

Images taken of the ACR phantom for a conventional x-ray tube source and a monoenergetic synchrotron beam without the analyser are shown in figures 3(*a*) and 3(*b*) respectively. The synchrotron radiographs typically showed an increase in contrast compared with images from the conventional system (Johnston *et al* 1996). The conventional radiographs was taken with a Siemens Mammomat 2 using Fuji mammography film (UM MA-HC), Fuji screen (UM Fine), and grid (4:1 ratio 27 lines/cm). The ACR image was obtained at 25 kVp, phototimed, 60 mA s. The synchrotron radiograph, figure 3(*b*), was obtained with the synchrotron set-up described in section 3 above, except that the analyser crystal was removed to allow a radiograph to be taken of the ACR phantom and the vertical beam size was increased to 0.5 mm. The image was taken at 18 keV x-ray energy, with 43 μC kg^{-1} exposure to the phantom. The scanning speed was 5.33 mm s^{-1} with an exposure time of 16.7 s. A Fuji ST5 image plate was used to record the image.

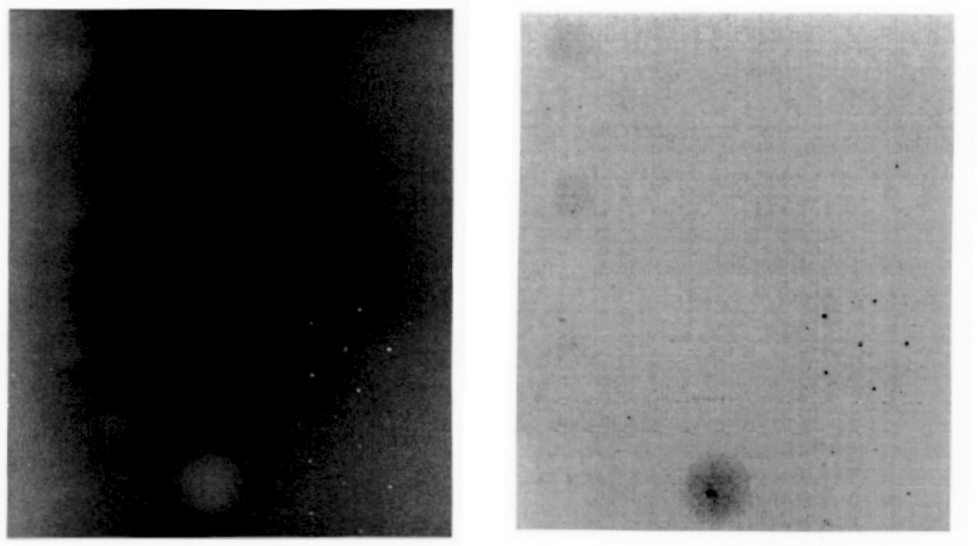

(*a*) (*b*)

Figure 3. Images of the ACR phantom. (*a*) A conventional image taken with a Siemens Mammomat II (Siemens Medical Systems, Iselin, NJ) mammography x-ray machine operated at 25 kVp. (*b*) An image taken using monoenergetic synchrotron radiation at 18 keV without an analyser crystal in place.

The low- and high-angle Bragg analyser images are shown in figures 1(*b*) and 1(*c*) respectively. Each of these images were taken with an increased exposure to the phantom of 84 μC kg^{-1} to maintain the same exposure to the image plate due to the half-reflectivity of the analyser crystal. Variations in the exposure to the image plate occur due to our inability to achieve exactly the half-reflectivity point in the rocking curve. These images were acquired at a scan speed of 0.54 mm s^{-1} with an exposure time of 165 s. The exposures were made onto a Fuji HR5 image plate.

Careful inspection of the images in figure 1 show that the edges of features in the images are enhanced and highlighted as if a shadow is cast on a three-dimensional surface. This shadowing effect is reversed between the images. This is most visible from the two

fibrils at the top right corners of the images. This effect is due to the images being taken on opposite slopes of the rocking curve. Coherent, incoherent and small-angle scattering outside the rocking curve (I_D diffraction) are not present in these images, leaving only the beam affected by apparent absorption and refraction (I_R from equation (1)). Any rays which deviate by even a few μrad from the incident direction and/or which deviate in energy by more than a few eV from the energy of the incident beam will not be diffracted by the analyser. It is clear that the images in figure 1 taken with the analyser have vastly superior contrast compared with the images in figures 3(*a*) and (*b*).

Figures 4(*a*) and (*b*) show the apparent absorption image, I_R, and the refraction angle image, $\Delta\theta_Z$, calculated from the decomposition algorithm (equations (6*a*) and (6*b*) applied to the images shown in figures 1(*b*) and (*c*). Since these images are derived from the two Bragg images, they are also scatter free.

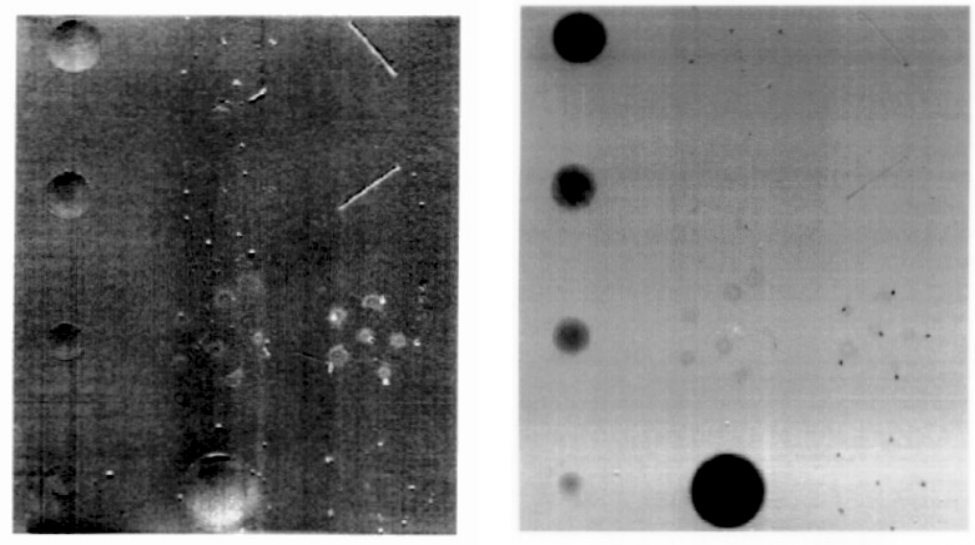

(*a*) (*b*)

Figure 4. The decomposed images obtained from the images in figures 1(*b*) and (*c*) using equations (6*a*) and (6*b*). (*a*) The refraction angle image. (*b*) The apparent absorption image.

The refraction image is, in effect, an image of the gradient of the refractive index of the object and hence capable of delineating very clearly the boundaries of regions in the object where the refractive index changes sharply. In effect, this produces an image edge enhancement in the Bragg images. Contrast in the refraction image arises from refractive index gradients along the beam path. This explains the three-dimensional shadowed look of the image. A good example of the refraction is to inspect the fibril simulation in the upper right-hand corner of figure 4(*a*). This object is a right circular cylinder and acts like a cylindrical lens. Thus the upper half will refract the x-rays in the opposite sense from the lower half. The refraction image is very useful in highlighting boundaries or edges in heterogeneous regions within the object. One may thus expect the refraction image to be highly useful in non-destructive examination of microcracks or other types of minute flaws.

The I_R image is a map of the intensity remaining after all the loss mechanisms have been taken out. Virtually all scatter is missing except for a small portion which falls within the angular acceptance of the analyser. The image is dominated by the apparent absorption

Table 1. Conventional and DEI contrast determination for a tumour simulation and a microcalcification from the American College of Radiology Quality Assurance Phantom.

Image	Exposure to phantom μC kg^{-1}	Embedded object	Signal[a]			Noise[a]	
			I	ΔI	$\Delta I/I$	δI	$\delta I/I$
Synchrotron radiograph (figure 3(*b*))	43	Tumour simulation	16.6	0.25	0.015	±0.10	±0.006
		Microcalcification	16.3	1.55	0.095	±0.09	±0.006
Synchrotron DEI (low-angle image, figure 1(*c*))	84	Tumour simulation	9.5	3.9	0.41	±0.28	±0.030
		Microcalcification	11.5	3.72	0.33	±0.17	±0.015
Apparent absorption image (combined image, figure 4(*b*))	168	Tumour simulation	18.8	7.6	0.40	±0.25	±0.013
		Microcalcification	21.3	5.13	0.24	±0.26	±0.012

[a] Values are taken from image plate data with no background subtraction. Data have been linearized using $I_{\mathrm{LINEAR}} = \exp(N_{\mathrm{RAW}}/255.0)$ where N_{RAW} is the raw data value.

which is normal absorption plus extinction. The ACR phantom is a good example of a material whose absorption and scatter are such that the sum in a normal transmission image (figure 3(*a*)) significantly degrades the contrast of the objects. For example, consider the simulated tumour mass in the upper left-hand corner of figure 3(*b*) and figure 4(*b*). The measured contrast of this 1.0 mm thick mass is summarized in table 1. The exposures used to obtain the images and the relative intensities measured from the images are shown. The relative intensities shown result from raw image plate data and are linearized since the raw data appear in 10-bit logarithmic form. The equation used to obtain the relative intensities is shown in the note to the table. The factor of 255 which divides the raw data value represents the gain setting of the logarithmic amplifier of the image plate reader. The relative intensities will then range from 1 to e^4(∼55). The I column values arise from the average background intensity in the vicinity of the embedded object. ΔI is the average change in intensity from the background in the middle of the object. Contrast is the ratio of these two values. The noise level, δ_I, is the standard deviation of the intensity, I (from the same region over which I has been averaged). The contrast measured from the synchrotron radiograph taken without an analyser in figure 3(*b*) gives a measured contrast of 1.5% $\Delta I_N/I_N$. However, the same mass in figure 1(*b*) taken on the low-angle side of the rocking curve gives a measured contrast of 41% $\Delta I_R/I_R$. The contrast of the apparent absorption image shown in figure 4(*b*) calculated using equation (6*a*) has a contrast of 40%. The diffracted beam images from the analyser alone have produced a contrast which is about 27 times greater than that in a synchrotron radiograph taken without an analyser! The apparent absorption image has similar contrast, but has a lower noise level since it results from a combination of two images.

The contrast has also been measured for the 0.54 mm diameter microcalcification simulation (largest of the star pattern dots above and to the right of the largest tumour simulation at the bottom of figures 1, 3 and 4). This microcalcification has a measured contrast of 9.5% in the synchrotron radiograph shown in figure 3(*b*). The image taken with the analyser, figure 1(*b*), has a measured contrast of 33%.

This startling contrast cannot be explained by normal absorption but is due to intensity loss caused by extinction. The mass created a significant amount of small-angle scatter which was removed from the Bragg diffracted images. This loss of intensity will appear as an apparent absorption within the object and hence as highly enhanced contrast in the image. It is suggested that this contrast enhancement effect be called extinction contrast.

The images in figure 4 demonstrate the usefulness of DEI for imaging objects based on their refraction properties and their ability to diffract (based on the spatial order or structure within the object). This raises the possibility of distinguishing between objects of the same elemental composition, but whose scattering properties are different based on structural order.

5. Conclusion

We believe that this new imaging technique may provide significant improvements in mammography and other areas of radiology, medical or non-medical. The unique ability of this system to provide an essentially scatter-free image of the object's apparent absorption as well as an image of the refraction effects may provide radiologists with sufficient additional information to allow detection of malignancies at an earlier stage than currently possible, even in patients with dense breasts. Since the ability of the monochromator and analyser system to resolve refraction effects and reject scattering does not depend on the imaging energy, there is a possibility that DEI may be optimally applied at higher x-ray energies, thus allowing dose reduction and in the case of mammography, less breast compression.

More studies using real tissues and anthropomorphic phantoms must be done to come to the conclusion that this technique can lead to a better method of breast imaging. There is the possibility that the enhanced contrast may detract from the ability detect cancerous tissue due the complexity of the structures involved. These issues will be the topic of future research.

Acknowledgments

The authors would like to thank Fuji Medical Systems for the loan of the AC3 image plate reader system and technical support in setting up and operating the unit. Also, we would like to thank Dr D Peter Siddons for the use of the X27C beamline and Ms B Dowd for assistance in setting up and operating the beamline. We thank Dr I Ivanov for preparing the analyser crystals used in these experiments. This work was supported in part by the State of Illinois Higher Education Cooperative Agreement, US Army grant DAMD17-96-1-6143 and at the National Synchrotron Light Source by US Department of Energy Contract DE-AC02-76CH00016 and ARPA contract AOB227.

References

Arfelli F, Burns C, Chapman D, Gmür N, Johnston R E, Menk R, Pisano E, Sayers D, Thomlinson W, Washburn D and Zhong Z 1995 *Brookhaven National Laboratory Informal Report* BNL-62935

Beliaevsky E A, Epfanov V P and Ingal V N 1991 Method for obtaining the image of the internal structure of an object *Soviet Patent* 4934958

——1992 Method for obtaining the image of the internal structure of an object *US Patent* 5319694

Burattini E, Cossu E, DiMaggio C, Gambaccini M, Indovina P, Marziani M, Porek M, Simeoni S and Simonetti G 1994 X-ray mammography with synchrotron radiation: a new high resolution technique valid for clinical application *Radiology* **195** 239–44

Chapman D, Thomlinson W, Arfelli F, Gmür N, Zhong Z, Menk R, Johnston R E, Washburn D, Pisano E and Sayers D 1996 Mammography imaging studies using a Laue crystal analyzer *Rev. Sci. Instrum.* **67** (published on CD-ROM)

Davis T J, Gao D, Gureyev T E, Stevenson A W and Wilkins S W 1995 Phase-contrast of weakly absorbing materials using hard X-rays *Nature* **373** 595–8

Davis T J, Gureyev T E, Gao D, Stevenson A W and Wilkins S W 1995 X-ray image contrast from a simple phase object *Phys. Rev. Lett.* **74** 3173–5

Johnston R E, Washburn D, Pisano E, Burns C, Thomlinson W C, Chapman L D, Arfelli F, Gmür N, Zhong Z and Sayers D 1996 Mammographic phantom studies with synchrotron radiation *Radiology* **200** 659–63

Margaritondo 1988 *Introduction to Synchrotron Radiation* (New York: Oxford University Press)

Nugent K A, Gureyev T E, Cookson D F, Paganin D and Barnea Z 1996 Quantitative phase imaging using hard x rays *Phys. Rev. Lett.* **77** 2961–4

Podurets K M, Somenkov V A and Shil'shtein S Sh 1989 Refraction-contrast radiography *Sov. Phys.–Tech. Phys.* **34** 654–7

Somenkov V A, Tkalich A K and Shil'shtein S Sh 1991 Refraction contrast in x-ray introscopy *Sov. Phys.–Tech. Phys.* **36** 1309–11

Thomlinson W 1992 Medical applications of synchrotron radiation *Nucl. Instrum. Methods* A **319** 295–304

——1994 Medical applications of synchrotron radiation at the National Synchrotron Light Source *Synchrotron Radiation in the Biosciences* ed B Chance *et al* (New York: Oxford University Press) pp 674–80

Wilkins S W, Gureyev T E, Gao D, Pogany A and Stevenson A W 1996 Phase-contrast imaging using polychromatic hard x-rays *Nature* **384** 335–8

Zachariasen W H 1945 *Theory of X-Ray Diffraction in Crystals* (New York: Wiley) ch 4

——1963 The secondary extinction correction *Acta Crystllogr.* **16** 1139–44